NASA Technical Memorandum 88887

Primary Arm Spacing in Chill Block Melt Spun Ni-Mo Alloys

S.N. Tewari and T.K. Glasgow
Lewis Research Center
Cleveland, Ohio

Prepared for the
Symposium "Enhanced Properties in Structural Metals via Rapid Solidification"
sponsored by the American Society for Metals
Orlando, Florida, October 6, 1986

NASA

PRIMARY ARM SPACING IN CHILL BLOCK MELT SPUN Ni-Mo ALLOYS

S.N. Tewari* and T.K. Glasgow
National Aeronautics and Space Administration
Lewis Research Center
Cleveland, Ohio 44135

SUMMARY

Chill block melt spun ribbons of Ni-Mo binary alloys containing 8.0 to 41.8 wt % Mo have been prepared under carefully controlled processing conditions. The growth velocity has been determined as a function of distance from the quench surface from the observed ribbon thickness dependence on the melt puddle residence time. Primary arm spacings measured at the midribbon thickness locations show a dependence on growth velocity and alloy composition which is expected from dendritic growth models for binary alloys directionally solidified in a positive temperature gradient.

INTRODUCTION

Rapid solidification of metallic alloys is known to result in refined microstructure, extended solute solubility, reduced microsegregation, and formation of metastable phases. Chill block melt spinning has been extensively used to produce rapidly solidified thin ribbons of many alloys. Microstructure of these melt spun alloys is studied because the microstructure controls mechanical properties. Chill block melt spinning is inherently a very complex process with many variables, including alloy composition, wheel material, speed and surface finish, atmosphere, melt temperature, ejection pressure, melt flow rate, angle of melt jet impingement, etc. These determine the physical and microstructural properties of the ribbon. Several simplified approaches have been taken to model the chill block melt spinning process. Momentum boundary layer models (refs. 1 to 3) have treated melt spinning as a material flow problem to determine the foil width, and calculate the foil thickness from the known flow rate and wheel speed. These approaches however, can not shed any light on the microstructural variation with ribbon thickness, especially for crystalline ribbons. Process models based on solidification principles (refs. 4 and 5) on the other hand provide the possibility of understanding microstructural evolution, in addition to predicting ribbon dimensions. Correlation of ribbon thickness with solidification time (melt puddle residence time) has been recently reported for a vacuum cast nickel base superalloy (ref. 6). This correlation suggested that the ribbon formation can be assumed to occur under ideal cooling conditions at the melt-wheel interface, with the only heat transfer resistance being through the thickness of the solidified metal. This approach takes no special account of the cellular or dendritic growth front of an alloy; it assumes alloy growth is similar to plane front growth of a pure element.

---

*Visiting Associate Professor, Department of Chemical Engineering, Cleveland State University, Cleveland, Ohio 44115.

A range of microstructures, plane front, cellular and dendritic, is
observed across melt spun crystalline ribbons due to varying local solidifica-
tion conditions. Solidification during melt spinning has been treated both,
as growth of the solid in an undercooled melt puddle (negative temperature
gradient ahead of the liquid-solid interface) (refs. 7 to 9) and as steady
state growth of the solid-liquid interface in the melt with a positive thermal
gradient (refs. 10 to 12). Prior studies of cellular/dendritic microstructures
have concentrated on refinement of the secondary dendrite arm spacing in melt
spun alloys (refs. 13 and 14). Unlike the secondary arm spacing, which is
known to change by Ostwald ripening related dendritic coarsening, the primary
arm spacing in the microstructure is stable. However, evolution of primary
dendrite arm spacing during rapid solidification has previously received very
little attention. Narayan (ref. 15) observed a good correlation between the
observed cell spacing and the minimum wave length for instability predicted by
the "absolute stability" (ref. 16) criterion for the laser annealed silicon
alloys. Boetinger et al. reported the scan velocity dependence of the primary
dendrite arm spacing for electron beam melted and resolidified Ag-Cu alloy
(ref. 17). Fayard et al. (ref. 18) have recently reported the dependence of
primary arm spacing on the nature of solute for the chill block melt spun
(CBMS) nickel base binary alloys. They however, observed that the primary
dendrite arm spacing remained the same across the ribbon thickness. No sys-
tematic study has been reported for examining the variation of the primary arm
spacing across the CBMS ribbon thickness or the dependence of arm spacing on
the alloy composition.

Several groups of dendritic growth models have been proposed to explain
the cellular/dendritic morphologies of binary alloys directionally solidified
in a positive thermal gradient (refs. 19 to 25). These models attempt to pre-
dict the dendrite tip radius (r_t), dendrite tip temperature (T_t) and the com-
position of the liquid at the dendrite tip (C_t) as a function of thermal gra-
dient at the dendrite tip (G), the alloy growth speed (R), solute content of
the alloy (C_0) and the alloy's physical properties. Morphological prediction
(r_t) can then be incorporated in primary dendrite arm spacing models, e.g.,
the model due to Hunt (ref. 26) to predict the dependence of the primary den-
drite arm spacings (λ_1) on alloy growth parameters. Comparison has been made
between data from the literature for directionally solidified binary alloys
and two types of dendrite growth models (ref. 27). For low growth velocities,
both dendrite models developed by Trivedi, [MS(T)] (ref. 23), based on the
morphological stability criterion applied at an Ivantsov dendrite tip, and the
model developed by Laxmanan, [MU(L) (ref. 24), based on the minimum under-
cooled dendrite tip approach, showed good fit to the data (ref. 27). Trivedi
has recently proposed a modification of his model (ref. 23) to incorporate the
asymmetric solute and thermal fields ahead of the dendrite tip for the high
growth velocity regime (ref. 12).

The purpose of this study was to investigate the dependence of the micro-
structural features of CBMS binary alloys on processing conditions. Nickel
rich Ni-Mo alloys were selected for this study because of relatively high par-
titioning coefficient value for this system (ref. 28). The high partitioning
coefficient is expected to lead to "absolute stability" controlled plane front
solidification at growth velocities which are considerably lower than that for
alloys with low partitioning coefficients. Since the partitioning coefficient
changes significantly in the vicinity of growth velocity, D/l, where D is
solute diffusivity in liquid and l is length of the order of interatomic
dimension, lower growth velocity experiments (R < 1 m/sec) are expected to be

free from the complications due to solute trapping. Growth velocity during melt spinning of nickel-molybdenum binary alloys has been obtained from the observed relationship between the ribbon thickness and the melt puddle residence time. Microstructures at the quench surface, midribbon thickness and free surface of the melt spun ribbons were examined by Transmission electron microscopy (TEM). Primary arm spacings at the midribbon thickness and free surface have been measured for ribbons produced under carefully controlled and reproducible melt spinning conditions. Dependence of the primary arm (intercellular) spacing on the growth velocity and alloy composition was examined and compared to the behavior expected from the dendrite growth models.

EXPERIMENTAL

Approximately 14 gm charges of the required composition (elemental nickel and molybdenum, 99.9 percent purity) were in-situ vacuum induction melted in 12 mm ID recrystallized alumina crucible used in the chill block melt spinning equipment (ref. 29). The alloy melts were homogenized for ten minutes at a superheat of 100 K. These were then cooled to approximately 50 K superheat above the liquidus temperature and ejected on to rotating 4340 alloy steel wheel surface. Alumina sheathed Pt-Pt 13 percent Rh thermocouples immersed in the melt were used to measure pouring temperature. The 18 cm diameter wheel surface was polished by 600 mesh SiC paper and cleaned by alcohol before each run. The melt, ejected with a positive pressure of argon (8.6×10^4 N/m^2) through an orifice of 1 mm diameter, impinged normal to the wheel surface from a distance of 2 cm. The melt puddle shapes for each run were recorded by a video camera. Puddle lengths were measured from 5 to 6 random television images for each processing condition, and averaged to obtain the puddle residence time on the quench wheel. Wheel surface speeds of 10, 20, and 40 m/sec were used. The melt spun ribbons were examined by optical and transmission electron metallography. The ribbon thicknesses were measured from optical micrographs and the average obtained from eight random specimens cut from the foil length. A Fishione twin jet polisher with an electrolyte consisting of sulphuric acid, hydrochloric acid and ethanol, in a ratio of 2: 0.5: 12 parts respectively, was used to thin the ribbons to prepare specimens for transmission electron metallography. Specimens were polished at 258 K, 35 V, and 20 mA. Care was taken to ensure that the ribbons polished at an equal rate from both the sides to obtain the exact ribbon midthickness region for the microscopic observations. TEM specimens for the free surface and the quench surface of the ribbons were prepared by masking the desired side of the ribbon with a laquer paint and polishing only from the other side. Primary arm spacings were measured for alloy specimens from three different TEM foils and the average value was obtained from 200 measurements. Chemical composition across the cells was measured by JEOL 100 STEM.

In separate experiments, alloy specimens of approximately 0.6 g were thermally conditioned (cycled between about 100 K above the alloy liquidus temperature and the solidification temperature) while immersed in a bed of pyrex/vycor glass in the recrystallized alumina crucible of a differential thermal analysis (DTA) unit in a flowing argon atmosphere. The undercooling (difference between alloy liquidus and the nucleation temperature) increased initially with the number of cycles and then became nearly constant. Specimens solidified from known levels of undercoolings were examined. Microsegregation across γ dendrites in such specimens was examined by electron microprobe analysis for comparision with melt spun samples.

3

RESULTS

Ribbon Thickness

Figure 1 shows the variation in the shape of the melt puddle during melt spinning of Ni-26 wt % Mo alloy as a function of wheel speed (circumferential). The melt puddle length in contact with the wheel surface decreases with increasing wheel speed. The melt puddle is bulged on the side opposite to the ribbon extraction. The extent of this bulging decreases with increasing wheel speed. The melt jet stream is symmetric in nature and impinges normal to the wheel surface. The length of the melt puddle in contact with the wheel surface measured from such figures can be used to calculate the puddle residence time from the known wheel speed, in the manner used by Huang et al. (ref. 6).

Figure 2 shows the variation in ribbon thickness and microstructure across the melt spun ribbons for the Ni-26 wt % Mo alloy cast at 10, 20, and 40 m/sec. The grains appear to grow normal to the wheel surface (on the quench side of the ribbons) for some distance (fig. 2(b) and (c)), before bending in the direction of the wheel surface velocity. A closer examination of structure within the grains shows that the microstructure is cellular across the ribbon thickness (except for the region very close to the quench wheel surface where it is planar as will be seen later). The primary cells also show the bent orientation of the grains (fig. 2(b)). Contrary to the observation by Fayard et al. (ref. 18) that the primary dendrite arm spacing is constant across the ribbon thickness, this microstructure shows (fig. 2(a)) that the primary arm spacing increases with the increasing distance from the quench surface. The observation that long unbroken primary cells extend from the quench side to the free side of the ribbons (fig. 2) shows that solidification did not occur ahead of the advancing cellular liqiuid-solid interface. No abrupt increases in primary cell spacing were observed. No equiaxed grains or randomly oriented dendrites were observed in the free surface regions of the ribbons. The whole ribbon thickness must have therefore formed by solidification in a positive temperature gradient controlled by the heat transfer to the quench wheel. Melt puddle residence time on the wheel surface can therefore be assumed to be equal to the ribbon solidification time.

Figure 3 shows the correlation between the ribbon thickness (S) and the melt puddle residence time (solidification time, t). The error bars on these data show the range observed in the specimen thickness and the solidification time. Data are shown for only three wheel speeds, because 40 m/sec was the highest speed available, and the ribbons grown at speeds much lower than 10 m/sec had a large variation in ribbon thickness along the ribbon length, possibly due to the problem of melt drag. The data show a straight line fit on the log (S) versus log (t) plot. The relationship between the ribbon thickness and the solidification time is as follows,

$$S = (2.1 \times 10^{-3}) \quad (t, \text{sec})^{0.5} \quad m \qquad (1)$$

Even though we have only three data points the confidence in this relationship is enhanced by the fact that Huang et al. (ref. 6) have also reported similar relationship for their vacuum cast nickel base alloy. Due to material continuity requirements the above relationship can be used to obtain the solid-liquid interface growth velocity (R) as a function of the distance from the quench surface (d) by differentiating with respect to time, t,

$$\frac{dS}{dt} = R = 2.2 \times 10^{-6} \quad (d,m)^{-1} \quad (m/sec) \quad (2)$$

Using the above relationship the growth velocity can be calculated at mid-ribbon thickness for the melt spun alloys. The ribbon thickness is observed to be nearly same for all the alloy compositions examined in this study for ribbons grown at a wheel speed of 20 m/sec. Therefore the relationship given by equation (2) is used for all the compositions examined in this study. The above approach however, treats the observed cellular liquid-solid interface (with a mushy zone) as if it were a plane front solidification of a pure element.

Microstructure on the Quench Side of the Ribbon

Figure 4 shows the typical microstructures observed on the quench side of the ribbon. All the grains consist of only the nickel rich solid solution phase, γ. No NiMo(β) phase is observed for any of the alloy compositions examined. Two types of microstructures are observed in this region of the foil. One contains plane front solidified and occasionally twinned grains (fig. 4(a)). Ribbons with molybdenum contents of 26 wt % or higher have planar features running across the grains, fig. 4(b). These individual grains give a single crystal (single phase) diffraction patterns. These features were identified as planar faults lying on the (111) planes of the γ phase (ref. 30).

Cellular Microstructure

Effect of wheel speed. - Figure 5 shows the effect of wheel speed on the microstructures at midthickness location of the melt spun Ni-26 wt % Mo alloy. The contrast within each grain is due to the cellular microstructure. The cells are nickel rich solid solution phase, γ. These cells do not have any secondary branches, and hence will not be called dendrites. NiMo(β) phase particles located in the intercellular regions can be seen in this figure (appearing dark). No γ-β eutectic is observed at the intercellular regions. The primary arm spacing decreases with the increasing wheel speed.

Figure 6 shows the wheel speed dependence of the cellular microstructure at the free surface of the CBMS ribbon. There is a large decrease in the primary arm spacing with the increasing wheel speed. The cell boundaries are defined mainly by the NiMo (β) particles and the associated dislocations.

The primary γ intercellular spacings measured from the midribbon thickness and free surface locations of the Ni-26 wt % Mo alloy melt spun at wheel speeds of 10, 20, and 40 m/sec can be used to describe the dependence of primary arm spacing on the distance from the quench surface. This relationship is shown in figure 7. The data points denote the average primary arm spacing values (average of 200 measurements). The primary arm spacing increases with the increasing distance from the quench surface. Length of error bars in figure 7 is twice the standard deviation observed for the given specimen.

Effect of alloy composition. - Figure 8 shows the effect of molybdenum content on the cellular microstructure at midthickness locations of the melt spun ribbons grown at a wheel speed of 20 m/sec. The microstructure for

molybdenum contents of 14.8 wt % or less is not cellular. The grains have disclocation networks within them, but the cellular contrast observed in the alloys with higher molybdenumm content is absent in these alloys. This region of these alloys therefore must have solidified in a plane front manner. The volume fraction of the intercellular β phase also increases with the increasing molybdenum content. Specimens with molybdenum content less than 36 wt % have only isolated β particles at the cell boundaries (figs. 6(b) to 9(c)). Whereas, those with higher molybdenum content have almost a continuous film of β at the cell boundaries (fig. 9(d) and (e)). All the microstructures examined in this study have been cellular (No evidence of secondary branches (i.e., primary dendrites) is seen in any of the alloy specimens examined). Also no γ-β eutectic is observed.in any of the specimens examined. Dependence of the primary arm spacing (ribbon midthickness) on the alloy composition for the ribbons melt spun at 20 m/sec is shown in figure 9. The data points indicate the average values of and the error bars denote twice the observed standard deviation in primary cell spacings. There is a slight decrease in the primary cell spacing with the increasing molybdenum content of the alloy.

MICROSEGREGATION ACROSS γ CELLS/DENDRITES

Growth in Undercooled Melt Versus Under a Positive Temperature Gradient

Figure 10 shows the molybdenum concentration profile across γ cells/ dendrites. Figure 10(a) is for dendrites observed in a Ni-43 wt % Mo alloy solidified in the DTA unit from an undercooling (difference between the liquidus and the nucleation temperatures) of 130 K. The electron microprobe trace across a dendrite shows the dendrite core to be richer in solute than the outer region. Dendrites growing in an undercooled melt puddle are expected to have a solute rich core (ref. 31) for alloys with solute partitioning coefficient (k) less than one, as is the case with Ni-Mo alloys examined in this study. For deep undercoolings the first solid to form is of same composition as the melt. During recalescence the solid forming has the same composition until the solidus temperature, (or "To" temperature, the temperature at which the free energies of the solid and liquid of the same composition are equal, as has been proposed by another approach (ref. 32)) is reached. The subsequent solid forming follows the equilibrium solidus till the maximum recalescence temperature is reached. During subsequent cooling further formation of the solid follows the solidus composition until the nucleation and growth of eutectic. The γ dendrites are therefore expected to solidify with a solute rich core and a solute poor outer region. However, this original microsegregation profile may not be retained. Diffusion during solidification and during cooling after the recalescence tends to homogenize the sample. Despite such homogenization the microsegregation trend (i.e., core with a higher solute content and outer region with a lower solute content) is clearly retained in the Ni-43 wt % Mo alloy specimen (fig. 10(a)). Such behavior has been experimentally observed for several binary alloys solidified from undercooled melts (ref. 31). On the other hand the directional solidification of a binary alloy in a positive temperature gradient in the liquid is expected to have the usual microsegregation (ref. 19), i.e., solute poor core (for k < 1). The STEM microchemical analysis across γ cells in a CBMS rapidly quenched Ni-41.8 wt % Mo alloy shows a molybdenum poor core (fig. 10(b)). None of the CBMS alloy ribbons examined in this study showed γ cells with a higher molybdenum content in the core as compared to their outer periphery. Therefore the cellular growth in this alloy system is not due to growth in an undercooled melt puddle

6

but is due to the directional solidification with a positive temperature gradient at the liquid solid interface. A similar conclusion has been drawn from microsegregation examination across an aluminum dendrite in a melt spun Al-Cu alloy (ref. 10). No information is available to judge whether the planar front portion grew into an undercooled melt.

ANALYSIS

Growth Speed (R) and Thermal Gradient (G)

The dendritic growth models for a solid growing in a positive temperature gradient in a binary alloy melt can be used to obtain the theoretical predictions for the primary arm spacing and the microsegregation across the cells in melt spun nickel-molybdenum alloy ribbons examined in this study. However, this requires an independent knowledge of G and R, besides the physical properties of the alloy system. Both G and R are expected to vary from the quench surface to the free surface region of the melt spun ribbons during solidification. There is no exact analytical treatment available in literature for heat flow during solidification of a binary alloy melt with a mushy zone against a chill surface. Caldwell et al. (ref. 33) carried out a numerical analysis of the problem. Lipton et al. have proposed an approximate analytical treatment of directional solidification with mushy zone (ref. 34). Solidification behavior of an alloy melt against a chill surface with a mushy liquid-solid zone has been treated by Huang et al. as the solidification of a pure element melt (ref. 6). Using this approach, Huang et al. showed that the ratio, G/R, can be assumed to be constant across the ribbon thickness during solidification of their melt spun nickel base superalloy ribbons. In this study also we will assume that G/R remains constant throughout the process of ribbon solidification for all the nickel-molybdenum alloys examined in this study. Based on the experimental observation that the ribbon thickness and the melt puddle residence time are the same for all the nickel-molybdenum alloy ribbons melt spun at the wheel speed of 20 m/sec we will also assume that the relationship between the growth speed and the distance from the quench surface obtained for the Ni-26 wt % Mo alloy (eq. (2)) is also valid for other compositions examined in this study.

Following Huang et al.'s argument that, $G/R = (T_p - T_{sl})/\alpha$, where T_p is alloy pouring temperature, T_{sl} is solid-liquid interface temperature and α is the thermal diffusivity of the liquid we can obtain the ratio G/R for our ribbons. In order to make use of the above relationship for an alloy freezing with a mushy zone where the temperature in the mushy zone varies from the eutectic temperature to a temperature slightly below the liquidus temperature (due to the dendrite tip undercooling), we will assume that T_{sl} can be taken to be the average temperature in the mushy zone, i.e., $T_{sl} = (T_{liquidus} + T_{eutectic})/2$, and estimate α_{eff} for the mushy zone in the following manner,

$$a_{eff} = \frac{K}{\rho\left[C_p + \frac{H}{\Delta T}\right]} \tag{3}$$

7

where

K   thermal conductivity of liquid = 0.74 w/cm K[1]

Cp   heat capacity of liquid = 0.62 J/g K

H   heat of fusion = 301 J/g

ΔT $(T_{liquidus} - T_{eutectic})$

ρ density of liquid = 7.905 g/cc

The G/R values obtained by the above procedure have been used to obtain the thermal gradient, G for the given growth velocity (R). G/R = 5.26×10^3 K sec/cm^2 was thus estimated for Ni-26 wt % Mo alloy.

Primary Arm Spacing

The dendrite tip radius predictions from the dendrite growth models can be incorporated into the primary arm spacing model due to Hunt (ref. 26). Such an approach showed that both the dendritic growth models mentioned above, MS(T) and MU(L), predicted a good quantitative fit to the experimental data in the low growth velocity regime (ref. 27). The theoretical relationships between the primary arm spacing and the experimental variables, as predicted from the above two dendrite growth models are given in ref. 27.

DISCUSSION

Primary Arm Spacing

<u>Effect of distance from the quench surface</u>. - The solid line in figure 7 shows the primary arm spacing values predicted for the Ni-26 wt % Mo alloy when the dendrite tip radius predictions from Laxmanan's minimum undercooled dendrite approach are used in the Hunt's primary arm spacing model (ref. 26). The slope of the theoretically predicted solid line in figure 7 is in very good agreement with the experimentally observed behavior. Considering the uncertainties in the assumed physical properties and other parameters the theoretical predictions show a reasonable fit to the observed primary arm spacing data.

One can force a much better fit to the experimental data with the theoretically predicted primary arm spacings if one uses a G/R value which is 5.5 times the actual estimated value of 5.26×10^3 K sec/cm^2. The broken line in figure 7 shows the theoretical predictions thus obtained from the MU(L) approach. For this same higher G/R value the model due to Trivedi,

---

[1]0.74 w/cm K is the liquid thermal conductivity of pure nickel (ref. 35). Thermal conductivity of solid nickel alloys (ref. 36) is 30 to 50 percent of the values reported for pure nickel (ref. 35). Effect of alloying on the liquid thermal conductivity is not known. However, if the alloy melt conductivity is lower then it would result in a higher value of 'G'.

based on the marginal stability at the paraboloidal dendrite tip (ref. 12), yields the broken line (fig. 8), employing the experimentally observed growth speed variation (eq. (2)). Both these dendrite growth theories yield a good fit to the experimentally observed primary arm spacing variation as a function of distance from the quench wheel surface when we assume constant, but higher than estimated, G/R and use the experimentally observed growth speed variation across the ribbon thickness. This higher G/R is not unreasonable considering the uncertainties in the physical properties of the alloy utilized for estimating G/R.

Effect of alloy composition. - The solid line in figure 9 shows the MU(L) theoretical predictions for the composition dependence of the primary arm spacings of the Ni-Mo alloys melt spun at a wheel speed of 20 m/sec. The quantitative predictions for the primary arm spacing (solid line in fig. 9) made by incorporating MU(L) dendrite tip radius predictions into Hunt's primary dendrite arm spacing shows a qualitative agreement with the experimentally observed behavior. Again G/R values, 5.5 times higher than those actually estimated yield a very good fit to the observed experimental data (broken line from MU(L) and chained line from MS(T)).

CONCLUSIONS

Chill block melt spun ribbons have been prepared from nickel-molybdenum binary alloys with molybdenum contents from 8.0 to 41.8 wt % under carefully controlled experimental conditions. Melt puddle residence time, ribbon thickness, microstructures across the ribbon thickness and microsegregation are examined as a function of alloy composition and wheel speed. The following conclusions can be drawn from this investigation.

1. Ribbon thickness (S) has a parabolic dependence on the melt puddle residence time (solidification time, t),

$$S = (2.1 \times 10^{-3}) \quad (t, sec)^{0.5} \quad m$$

2. The solidification during melt spinning is not due to growth of the solid (at least for cellular structure) in an undercooled melt puddle; but is due to the growth of the solid-liquid interface in a positive temperature gradient.

3. The growth speed (R) has the following relationship with the distance from the quench surface, d,

$$\frac{dS}{dt} = R = 2.2 \times 10^{-6} \quad (d, m)^{-1} \quad (m/sec)$$

4. Microstructure at the quench surface of the ribbon is due to the segregation free plane front solidification of nickel rich solid solution phase, γ. Alloys with molybdenum contents from 26 to 41.8 wt % Mo produce γ grains with planar faults.

5. The microstructure in rest of the ribbon consists of γ cells with intercellular β (NiMo) precipitates. No γ-β eutectic is observed in the

melt spun specimens examined in this study. No evidence of secondary branching is observed.

6. The intercellular (primary arm) spacing increases with the distance from the quench wheel. The primary arm spacing at midribbon thickness shows a slight decrease with increasing molybdenum content.

7. Two dendrite growth models for binary alloys directionally solidified in a positive temperature gradient, one due to Laxmanan, MU(L) (based on a Zener type of approach with minimum undercooling at the dendrite tip) and the other due to Trivedi, MS(T) (based on marginal stability at an Ivantsov type of parabolloidal dendrite tip), have been examined. Both these models coupled with the primary dendrite arm spacing model of Hunt show a reasonable fit to the observed dependence of primary arm spacing on distance from the quench surface and on the alloy composition.

ACKNOWLEDGEMENT

REFERENCES

1. J.H. Vincent, J.G. Herbertson, H.A. Davies: in Rapidly Quenched Metals IV, T. Masumoto and K. Suzuki, eds., The Japan Institute of Metals, Sendai, 1982, pp. 77-80.

2. H.H. Liebermann: Mater. Sci. Eng., 1980, vol. 43, pp. 203-210.

3. J.H. Vincent, J.G. Herbertson, and H.A. Davies: J. Mater. Sci. Lett., 1983, vol. 1, pp. 88-90.

4. S. Kavesh: in Metallic Glasses, J.J. Gilman and H.J. Leamy, eds., American Society for Metals, Metals Park, OH, 1976, pp. 36-73.

5. V. Laxmanan: in Rapidly Solidified Metastable Materials, B.H. Kear and B.C. Giessen, eds., North Holland, New York, 1984, pp. 21-27.

6. S.C. Huang, R.P. Laforce, A.M. Ritter, and R.P. Goehner: Metall. Trans. A, 1985, vol. 16, pp. 1773-1779.

7. H. Jones: Mater. Sci. Eng., 1984, vol. 65, pp. 145-156.

8. C. Hayzelden, J.J. Rayment, and B. Cantor: Acta Metall., 1983, vol. 31, pp. 379-386.

9. P.G. Boswell and G.A. Chadwick: Scr. Metall., 1977, vol. 11, pp. 459-465.

10. L.J. Masur and M.C. Flemings: in _Rapidly Quenched Metals IV_, T. Masumoto and K. Suzuki, eds., Vol. 2, The Japan Institute of Metals, Sendai, 1982, pp. 1557-1560.

11. L. Katgerman: _Scr. Metall._, 1983, vol. 17, pp. 537-540.

12. R. Trivedi: _J. Crystal Growth_, 1985, vol. 73, pp. 289-303.

13. W.E. Brower Jr., R. Strachan, and M.C. Flemings: _Cast Met. Res. J._, 1970, vol. 6, pp. 176-180.

14. A. Munitz: _Metall. Trans. B_, 1985, vol. 16, pp. 149-161.

15. J. Narayan: _J. Crystal Growth_, 1982, vol. 59, pp. 583-598.

16. W.W. Mullins and R.F. Sekerka: _J. Appl. Phys._, 1964, vol. 35, pp. 444-451.

17. W.J. Boettinger, D. Shechtman, R.J. Schaefer, and F.S. Biancaniello: _Metall. Trans. A_, 1984, vol. 15, pp. 55-66.

18. F. Fayard, F. Duflos, A. Lasalmonie: in _Rapidly Quenched Metals_, vol. 1, S. Steeb and H. Warlimont, eds., North Holland, New York, 1985, pp. 811-814.

19. H.D. Brody and M.C. Flemings: _Trans. AIME_, 1966, vol. 236, pp. 615-623.

20. M.H. Burden and J.D. Hunt: _J. Crystal Growth_, 1974, vol. 22, pp. 109-116.

21. J.S. Kirkaldy: _Scr. Metall._, 1980, vol. 14, pp. 739-744.

22. W. Kurz and D.J. Fisher: _Acta Metall._, 1981, vol. 29, pp. 11-20.

23. R. Trivedi: _J. Crystal Growth_, 1980, vol. 49, pp. 219-232.

24. V. Laxmanan: _Acta Metall._, 1985, vol. 33, pp. 1037-1049.

25. I. Jin and G.R. Purdy: _J. Crystal Growth_, 1973, vol. 23, pp. 29-44.

26. J.D. Hunt: _Solidification and Casting of Metals_, The Metals Society, London, 1979, pp. 3-9.

27. S.N. Tewari and V. Laxmanan: A Critical Examination of the Dendrite Growth Models: Comparison of Theory with Experimental Data," To appear in _Acta Metall._, 1986.

28. Metals Handbook, 8th ed., Vol. 8, American Society for Metals, Metals Park, OH, 1973, p. 319.

29. R.W. Jeck, T.J. Moore, T.K. Glasgow, and N.W. Orth: _J. Met._, 1984, vol. 36, no. 4, pp. 41-45.

30. N. Jayaraman and S.N. Tewari: "Fault Structures in Rapidly Quenched Ni-Mo Alloys," To appear in _Metall. Trans._, 1986.

31. T.Z. Kattamis: _Z. Metalkd._, 1970, vol. 61, pp. 856-860.

32. M.G. Chu: Solidification of Highly Undercooled Alloy Droplets, Ph.D.
    Thesis, Massachusetts Institute of Technology, 1983.

33. T.W. Caldwell, A.J. Campagna, M.C. Flemings, and R. Mehrabian: Metall.
    Trans. B, 1977, vol. 8, pp. 261-270.

34. J. Lipton, A. Garcia, and W. Heinemann: Arch. Eisenhuettenwes, 1982,
    vol. 53, pp. 469-473.

35. Thermophysical Properties of Matter, vol. 1, edited by Y.S. Touloukian
    et al., IFI/Plenum,
    New York, 1970, pp. 242-244..

36. Nickel Alloy Steels Databook, 3rd ed., International Nickel Co., New York,
    1965, p. 19.

(A) 10 M/SEC   (B) 20 M/SEC   (C) 40 M/SEC
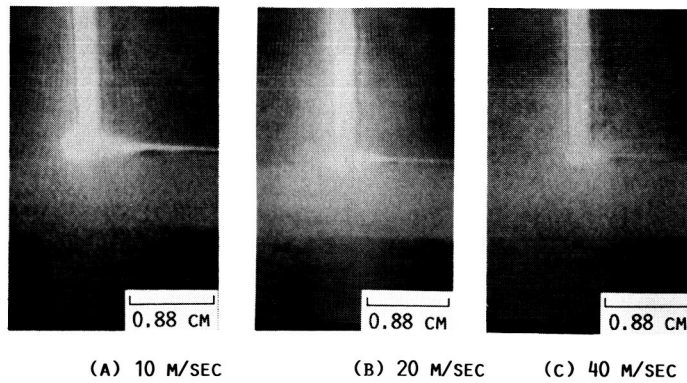
FIGURE 1. - DEPENDENCE OF THE MELT PUDDLE SHAPE ON THE WHEEL SPEED
FOR A NI-26 WT% MO ALLOY.

(A) 10 M/SEC.

(B) 20 M/SEC.

(C) 40 M/SEC.
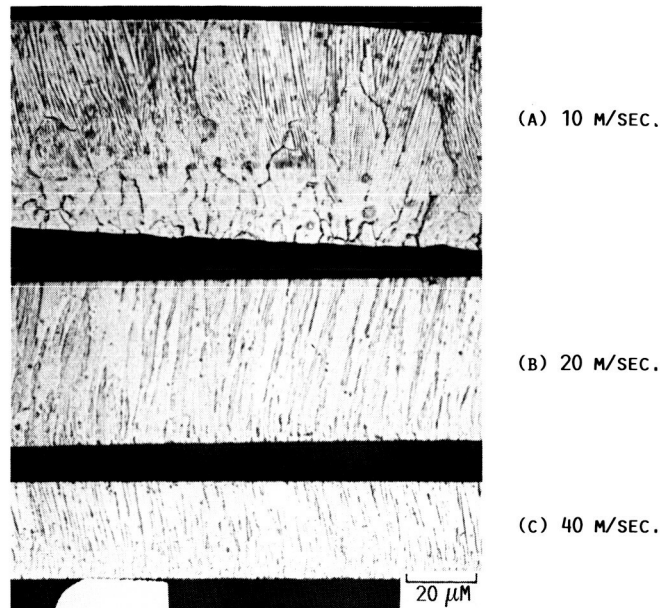
FIGURE 2. - EFFECT OF WHEEL SPEED ON THE RIBBON
THICKNESS AND MICROSTRUCTURE OF MELT SPUN NI-26
WT% MO ALLOY. QUENCH SIDE OF THE RIBBONS IS
AT BOTTOM.
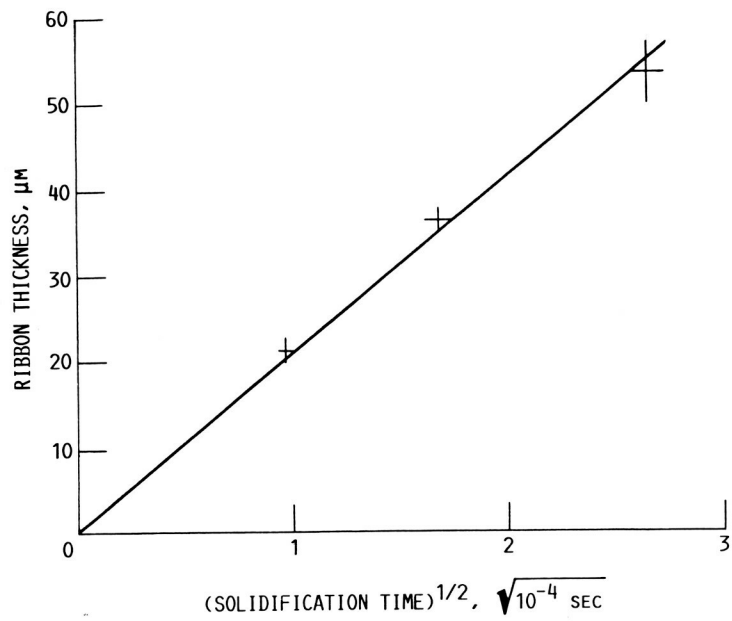
FIGURE 3. - CORRELATION BETWEEN RIBBON THICKNESS(S) AND MELT PUDDLE RESIDENCE TIME (SOLIDIFICATION TIME), t FOR NI-26 WT % MO ALLOY.

(A) NI-26 WT% MO

(B) NI-39.7 WT% MO

FIGURE 4. - EFFECT OF COMPOSITION ON THE QUENCH SIDE MICROSTRUCTURE OF THE CBMS RIBBON, SOLIDIFIED AT A WHEEL SPEEED OF 20 M/SEC.
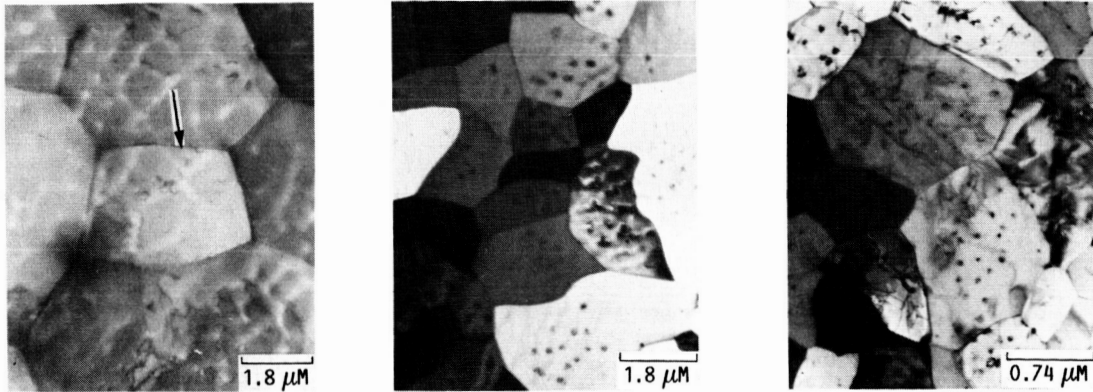
(A) 10 M/SEC.   (B) 20 M/SEC.   (C) 40 M/SEC.

FIGURE 5. - EFFECT OF WHEEL SPEED ON THE MID-THICKNESS OF MELT SPUN NI-26 WT% MO ALLOY RIBBONS.
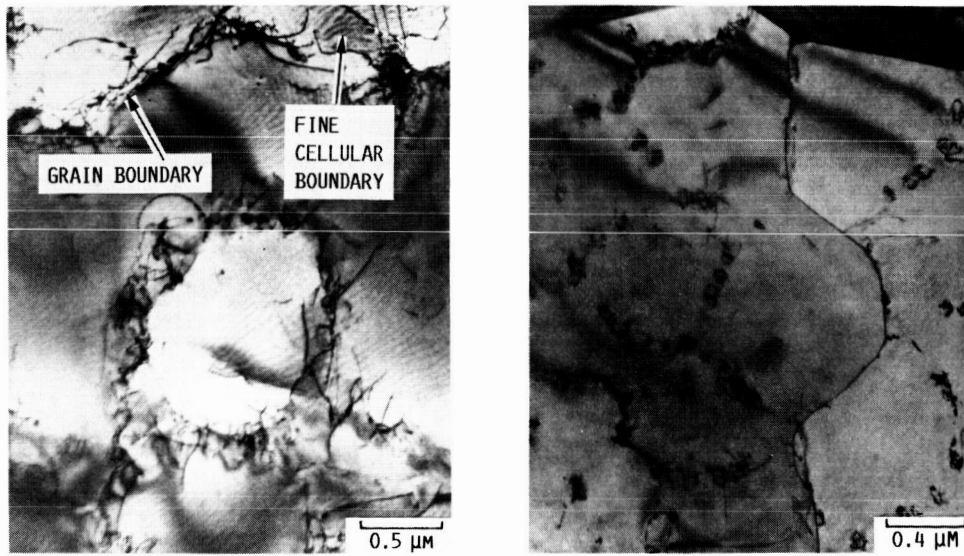
(A) 10 M/SEC.   (B) 20 M/SEC.

FIGURE 6. - EFFECT OF WHEEL SPEED ON THE MICROSTRUCTURE OF THE FREE SURFACE OF THE CBMS
RIBBON OF NI-26 WT% MO ALLOY.

(c) 40 M/SEC.

FIGURE 6. - CONCLUDED.
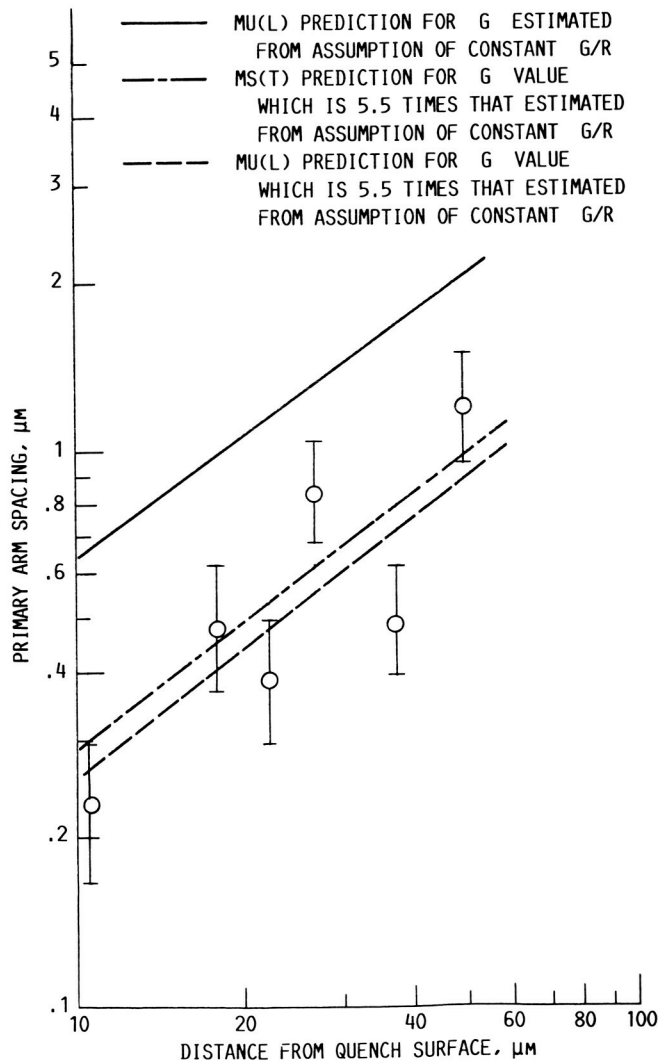
FIGURE 7. - VARIATION OF PRIMARY ARM SPACING WITH
DISTANCE FROM QUENCH SURFACE FOR NI-26 WT % MO
MELT SPUN RIBBON.

(A) 8.0 WT% MO.
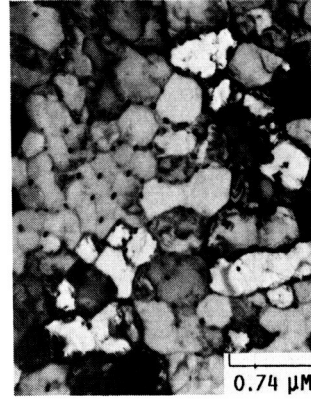
(B) 36.0 WT% MO.

FIGURE 8. - EFFECT OF ALLOY COMPOSITION ON THE MID-THICKNESS
MICROSTRUCTURES OF MELT SPUN NI-MO ALLOY RIBBONS.
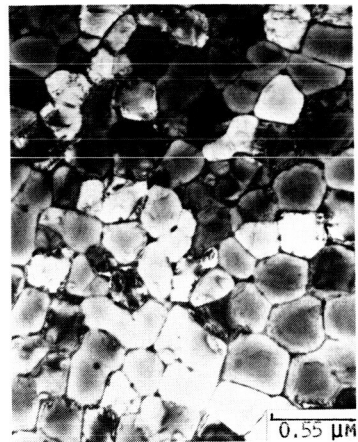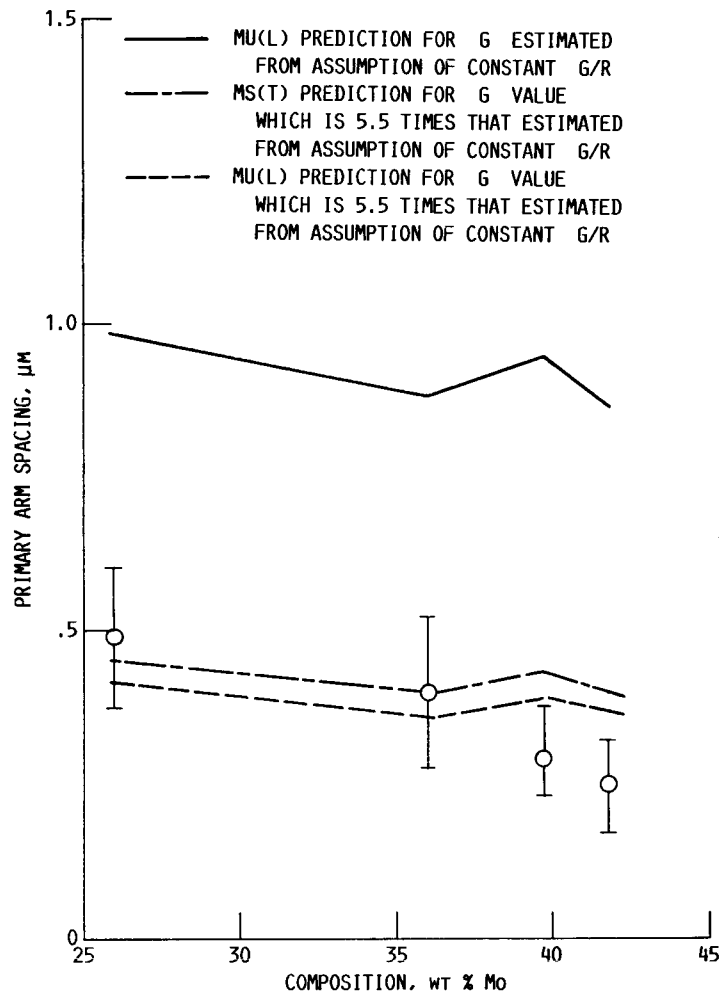

(C) 41.8 WT% MO

FIGURE 8. - CONCLUDED.

FIGURE 9. - VARIATION OF PRIMARY ARM SPACING WITH MOLYBDENUM CONTENT OF NI-MO ALLOYS (WHEEL SPEED = 20 M/SEC).

(A) IN AN UNDERCOOLED
NI-43 WT % MO ALLOY.

(B) IN A MELT SPUN NI-41.8
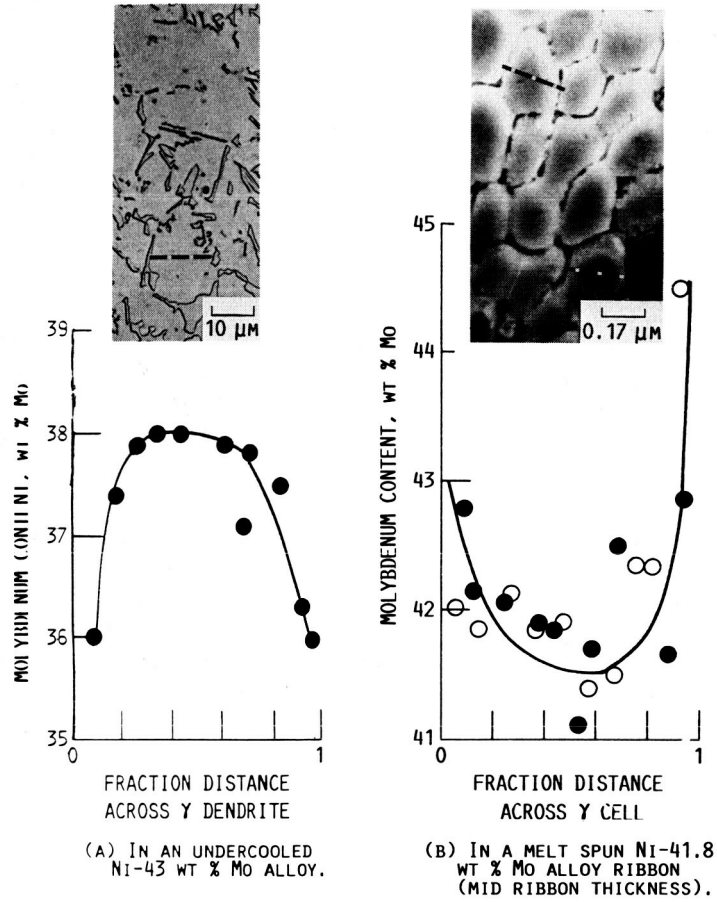WT % MO ALLOY RIBBON
(MID RIBBON THICKNESS).

FIGURE 10. - MICROSEGREGATION ACROSS γ DENDRITE/CELLS.
(● AND ○ ARE DATA FROM TWO CELLS IN THE SAME TEM
FOIL.)

1. Report No. NASA TM-88887	2. Government Accession No.	3. Recipient's Catalog No.
4. Title and Subtitle Primary Arm Spacing in Chill Block Melt Spun Ni-Mo Alloys		5. Report Date
		6. Performing Organization Code 674-25-05
7. Author(s) S.N. Tewari and T.K. Glasgow		8. Performing Organization Report No. E-3297
		10. Work Unit No.
9. Performing Organization Name and Address National Aeronautics and Space Administration Lewis Research Center Cleveland, Ohio 44135		11. Contract or Grant No.
		13. Type of Report and Period Covered Technical Memorandum
12. Sponsoring Agency Name and Address National Aeronautics and Space Administration Washington, D.C. 20546		
		14. Sponsoring Agency Code

16. Abstract

Chill block melt spun ribbons of Ni-Mo binary alloys containing 8.0 to 41.8 wt % Mo have been prepared under carefully controlled processing conditions. The growth velocity has been determined as a function of distance from the quench surface from the observed ribbon thickness dependence on the melt puddle residence time. Primary arm spacings measured at the midribbon thickness locations show a dependence on growth velocity and alloy composition which is expected from dendritic growth models for binary alloys directionally solidified in a positive temperature gradient.

17. Key Words (Suggested by Author(s)) Rapid quenching; Rapid solidification; Ni-Mo; Primary arm spacing	18. Distribution Statement Unclassified - unlimited STAR Category 26

19. Security Classif. (of this report) Unclassified	20. Security Classif. (of this page) Unclassified	21. No. of pages	22. Price*